Oxygen Transport and Free Volume in Cold-Crystallized and Melt-Crystallized Poly(ethylene naphthalate)

Y. S. Hu,[†] R. Y. F. Liu,[†] L. Q. Zhang,[†] M. Rogunova,[†] D. A. Schiraldi,[‡] S. Nazarenko,[†] A. Hiltner,*[,†] and E. Baer[†]

Department of Macromolecular Science and Center for Applied Polymer Research, Case Western Reserve University, 10900 Euclid Avenue, Cleveland, Ohio 44106-7202, and KoSa, 1551 Sha Lane, Spartanburg, South Carolina 29304

Received April 1, 2002; Revised Manuscript Received June 10, 2002

ABSTRACT: In the present study we examined the oxygen-transport properties of poly(ethylene naphthalate) (PEN) isothermally crystallized from the melt (melt crystallization) or quenched to the glass and subsequently isothermally crystallized by heating above the glass transition temperature (cold crystallization). The *gauche*/*trans* conformation of the glycol linkage was determined by infrared analysis, and the crystalline morphology was examined by atomic force microscopy (AFM). Explanation of the unexpectedly high solubility of crystallized PEN required a two-phase transport model consisting of an impermeable crystalline phase of constant density and a permeable amorphous phase of variable density. The resulting relationship between oxygen solubility and amorphous-phase density was consistent with free volume concepts of gas sorption. Morphological observations provided a structural model for solubility and permeability. The model consisted of a permeable amorphous matrix of constant density containing dispersed spherulites of lower permeability. The spherulites themselves were composites of impermeable crystallites and permeable interlamellar amorphous regions of lower density than the amorphous matrix. Dedensification of the interlamellar amorphous phase was due to the constrained nature of amorphous chains anchored to crystallites.

Introduction

Crystallization significantly improves the barrier properties of polymers.[1,2] The efficiency of chain packing is such that the crystalline phase is generally regarded as impermeable to even small gas molecules. Crystallization reduces solubility due to the smaller volume fraction of the permeable amorphous phase. Crystallization reduces diffusivity by increasing the diffusion pathway to an extent that depends on the shape and spatial arrangement of the impermeable crystals. Diffusivity is further affected if the mobility of amorphous chains is altered by attachment to crystals.

Impermeability of crystals is the basis of the simple two-phase transport model, which consists of an impermeable crystal phase dispersed in a permeable amorphous matrix.[3] According to the model, solubility should be a linear function of the amorphous volume fraction. This is confirmed for the solubility of small gases in polyethylene.[4] The solubility of water vapor in poly(ethylene terephthalate) (PET) and in polyamide 610 also conforms with the simple model.[5] However, the decrease in solubility of many gases including oxygen in poly(ethylene terephthalate) is smaller than predicted by the two-phase model.[6] It was proposed that crystallization tends to occur in the denser regions of the amorphous polymer, thus concentrating free volume in the remaining amorphous regions. More recently, the unexpectedly high gas solubility of crystalline PET and PET copolymers was addressed using the concept of a dedensified amorphous phase.[7−9] The two-phase model is formulated in terms of a crystalline phase of constant density, ρ_c, and an amorphous phase of variable density that depends on the volume fraction crystallinity, $\rho_a(\phi_c)$.

Other polymers related to PET also might not conform to the simple two-phase model. In the present study, the two-phase model is tested with crystallized poly(ethylene naphthalate) (PEN), a high-performance engineering plastic with excellent barrier properties. Like PET, PEN can be crystallized from the melt (melt crystallization), or alternatively it can be rapidly quenched to the amorphous glass and subsequently crystallized by heating above the glass transition temperature (cold crystallization). Isothermal crystallization of PEN is slow enough that the kinetics can be accessed easily over the entire bell-shaped curve.[10,11] Melt crystallization and cold crystallization proceed at similar rates by nucleation and growth of banded spherulites until the spherulites are space-filling. The Avrami plots exhibit a coefficient that is close to 3, and they do not deviate distinctly from linearity in the later stages of crystallization. These features are consistent with primarily 3-dimensional growth of heterogeneously nucleated spherulites having constant crystallinity.[12] On the basis of these characteristics, an attempt to seek a structural model for gas transport appears promising.

In the present study we test the formulation of the two-phase model for PEN by examining the effect of cold crystallization and melt crystallization on oxygen-transport properties. The amorphous phase of the crystallized polymer is analyzed in terms of free volume concepts of oxygen solubility previously developed for the oriented, densified glass. The crystalline morphology is examined to develop a structural model for oxygen transport.

Materials and Methods

PEN was provided by KoSa (Spartanburg, SC) in the form of extruded pellets. The intrinsic viscosity of the PEN pellets was 0.64 dL g^{-1}, measured at 25 °C in 1% (w/w) dichloroacetic acid solution. The diethylene glycol (DEG) content of the PEN

[†] Case Western Reserve University.
[‡] KoSa.

10.1021/ma0205156 CCC: $22.00
Published on Web 08/10/2002

was 0.96 mol %, determined by methanolysis of the polyester, followed by gas chromatography analysis for DEG. The pellets were dried in vacuo at 80 °C for 24 h prior to molding. Films 120−150 μm thick were obtained by compression molding the pellets between Teflon-coated aluminum sheets in a press at 310 °C. The platens were heated in the press for 5 min with repeated application and release of pressure to remove air bubbles, and held at 20000 psi for an additional 5 min. Amorphous films were obtained by quenching from the melt into cold water. Cold-crystallized barrier specimens were prepared by annealing amorphous films in an oven at the appropriate temperature, followed by quenching into cold water. Films were crystallized at 165 °C for various periods of time from 10 min to 13.5 h to obtain specimens that differed in the amount of crystallinity. Amorphous films were also cold-crystallized at 180 °C for 12 h and at 200 °C for 10 h to obtain higher crystallinities. For melt-crystallized barrier specimens, the melted films between Teflon sheets were transferred rapidly from the press at 310 °C to an oven at 220 °C, crystallized for various periods of time from 10 min to 4 h, and quenched into cold water.

Density was measured with a density gradient column constructed from an aqueous solution of calcium nitrate in accordance with ASTM-D 1505 method B. The column was calibrated with glass floats of known density. Small pieces of film (~25 mm^2) were placed in the column and allowed to equilibrate for 30 min before the measurements were taken. Thermal analysis was conducted with a Perkin-Elmer DSC-7. Heating scans were performed at 10 °C min^{-1} over the temperature range from 30 to 290 °C. The X-ray diffraction measurements were performed at ambient temperature with a Philips diffractometer in the transmission mode using a slit angle of 0.5°. Positron annihilation lifetime spectroscopy (PALS) was performed using a conventional fast−fast coincidence system. The instrumentation and procedures for data analysis were described previously.[13]

Conformational composition was determined by photoacoustic Fourier transform infrared (FTIR) spectroscopy. Spectra were collected at ambient temperature with a Nicolet 870 FTIR spectrometer using an MTEC model 200 photoacoustic cell. Specimens 10 mm in diameter were cut from the film after the barrier measurement. All infrared specimens were dried overnight in vacuo at ambient temperature to remove moisture. For each specimen, 256 scans were collected with a resolution of 4 cm^{-1} and mirror velocity of 0.158 cm s^{-1}. The 1500−1400 cm^{-1} region of the spectrum was deconvoluted into four Gaussian peaks using Origin 4.1 software. The fractions of *gauche*- and *trans*-glycol conformations were obtained from the relative peak heights.

For atomic force microscopy, specimens were sectioned with an ultramicrotome (MT6000-XL from RMC, Tucson, AZ) and etched for 30 min at ambient temperature in a solution of 10 mg of potassium permanganate/mL of a 10:4:3 v/v/v mixture of concentrated sulfuric acid, orthophosphoric acid (85%), and water.[14] The etched surfaces were examined in air at ambient conditions using the Nanoscope IIIa MultiMode head from Digital Instruments (Santa Barbara, CA) in the tapping mode. Phase and height images were recorded simultaneously.

Oxygen flux, $J(t)$, at 0% relative humidity, 1 atm of pressure, and 25 °C was measured with a MOCON OX-TRAN 2/20. Additional experiments were carried out at various temperatures in the range of 10−40 °C. Specimens were carefully conditioned as described previously,[7] to obtain the non-steady-state oxygen flux from which the diffusivity, D, was determined. The average thickness, l, of each specimen was determined as $l = W(A\rho)^{-1}$, where W is the sample weight, A is the sample area, and ρ is the density.

Results

Crystalline Morphology. The increase in crystallinity expressed as the density of PEN barrier films followed the typical sigmoidal dependence on isothermal crystallization time as shown in Figure 1. During the rapid increase in density the volume fraction occupied by spherulites increased by the processes of nucleation and growth.[10] The small increase in density at longer times after the spherulites were space-filling reflected secondary crystallization.

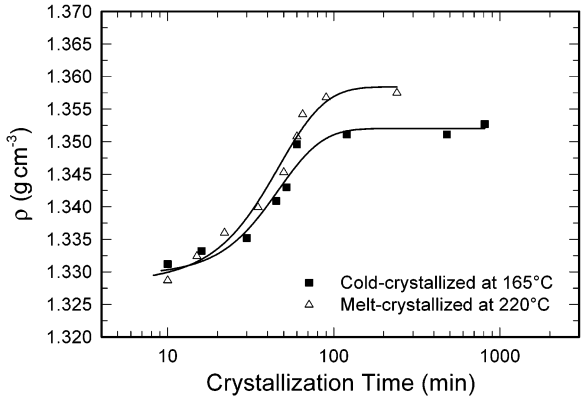

Figure 1. Crystallinity measured as density as a function of crystallization time.

An AFM phase image of a film melt-crystallized for 22 min at 220 °C displayed individual spherulites embedded in an amorphous matrix, Figure 2a. After 90 min at 220 °C space-filling spherulites characterized the completely crystallized film, Figure 2b. The spherulites exhibited a regular banding pattern with spacing of about 2.6 μm. Persistence of a constant band spacing during isothermal spherulite growth conformed with the general observation that the banding period is determined primarily by the crystallization temperature.[15] Cold crystallization for 8 h at 165 °C produced smaller space-filling spherulites than melt crystallization at 220 °C, which was consistent with a higher nucleation density, Figure 2c. The 0.38 μm banding pattern of cold-crystallized spherulites was much smaller than the band spacing of melt-crystallized spherulites in accordance with the general observation that band spacing decreases with crystallization temperature.[16,17]

Conformer Characterization. The infrared spectrum of PEN is well characterized.[18−20] Specific bands assigned to *trans* and *gauche* conformers of the glycol appear in three regions of the spectrum: 1500−1400, 1400−1300, and 1100−800 cm^{-1}. Bands at 1477 and 1456 cm^{-1} observed in both amorphous and crystalline PEN are associated with the CH_2 bending vibrations of *trans* and *gauche* configurations, respectively. Changes in the peak intensities of these two bands revealed the expected increase in *trans* conformers relative to *gauche* conformers with crystallization, Figure 3. These two peaks were used for quantitative determination of conformer populations.

Spectra were normalized to the carbonyl stretching band at 1730 cm^{-1},[21] and the 1500−1400 cm^{-1} region was deconvoluted into four Gaussian peaks as illustrated in Figure 4. The relative amounts of *gauche* and *trans* conformers were determined by plotting the normalized peak heights as in Figure 5. Excellent linearity was obtained. Extrapolation gave intercepts that corresponded to the normalized band intensities for 100% *trans* and 100% *gauche* conformers. It can be seen from the intercepts that the *gauche* and *trans* bands used in the analysis had about the same molar absorptivity.

The *trans* fraction, f_t, defined as the ratio of the normalized 1477 cm^{-1} peak height to the normalized

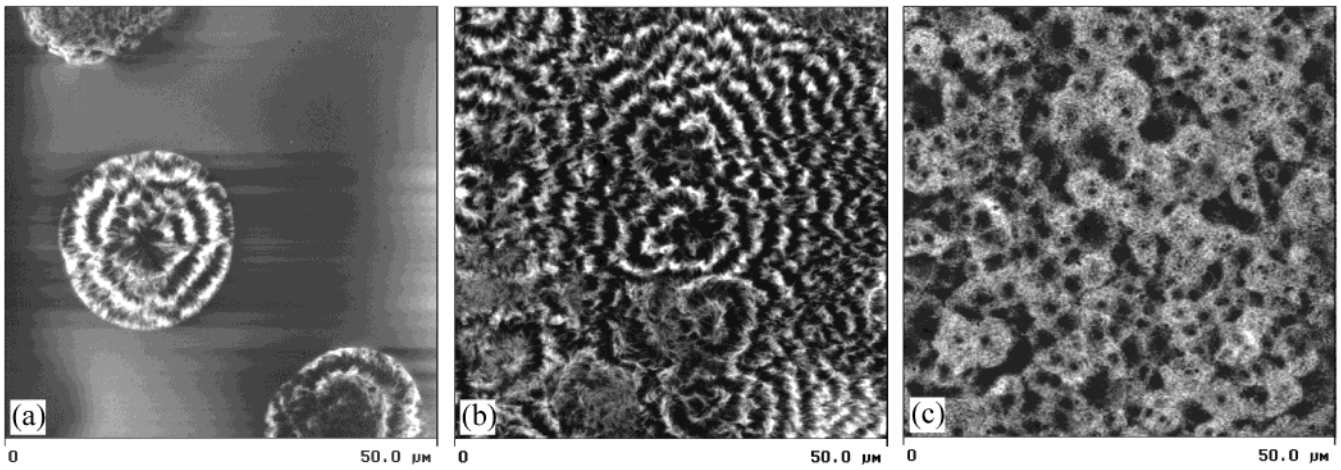

Figure 2. AFM phase images of PEN: (a) melt-crystallized at 220 °C for 22 min; (b) melt-crystallized at 220 °C for 90 min; (c) cold-crystallized at 165 °C for 8 h.

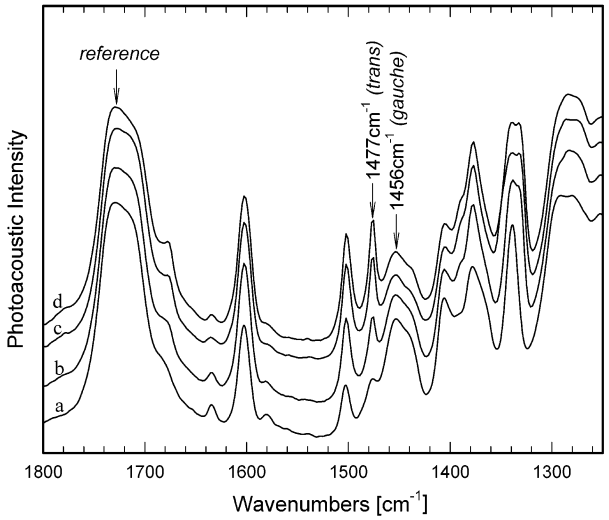

Figure 3. Representative FTIR spectra of PEN melt-crystallized at 220 °C for (a) 0 min, (b) 15 min, (c) 60 min, and (d) 240 min.

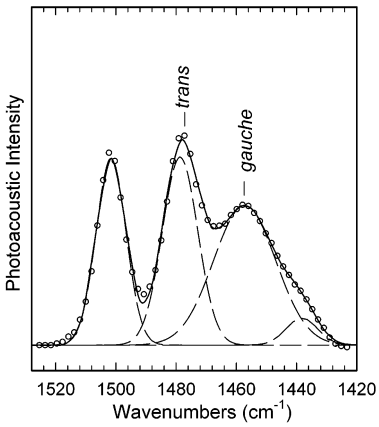

Figure 4. Deconvolution of the 1500−1400 cm^{-1} region of the infrared spectrum to obtain peak heights of *trans* and *gauche* bands for crystallized PEN.

1477 cm^{-1} peak height for 100% *trans* conformers was about 0.20 in an amorphous PEN film, which was higher than the *trans* fraction of 0.10 reported for amorphous PET.[21−23] The *trans* fraction increased with crystallinity,

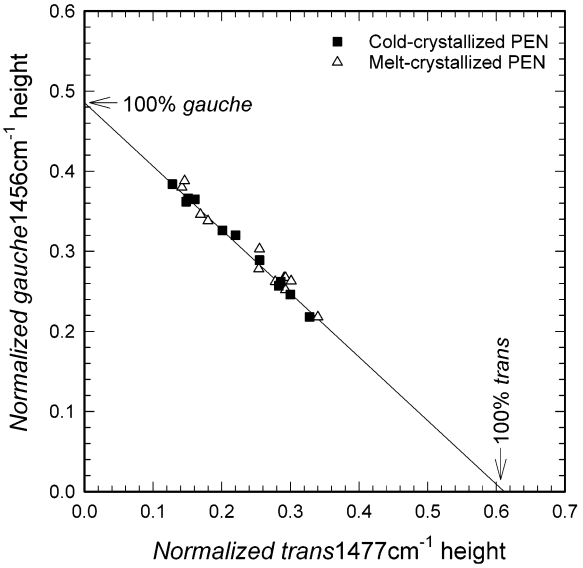

Figure 5. Normalized peak heights of the *gauche* and *trans* infrared bands of cold- and melt-crystallized PEN.

Tables 1 and 2. The relationship between the *trans* fraction and crystallinity as measured by ΔH, where ΔH is the sum of the endothermic melting enthalpy and the exothermic cold crystallization enthalpy in the DSC heating scan, is plotted in Figure 6. Extrapolation of the linear relationship gave 131 J g^{-1} as the heat of melting for PEN with 100% *trans* conformers. This value can be considered as $\Delta H°$ for the extended chain α-form PEN crystal. However, it is somewhat larger than the 104 J g^{-1} proposed in the literature.[24]

Oxygen Transport. Typical experimental curves in Figure 7 describe the oxygen flux, $J(t)$, through an amorphous PEN film and through several melt-crystallized PEN films of increasing crystallinity. To facilitate comparisons among specimens that varied somewhat in thickness, the flux curves were normalized to a film thickness of 200 μm. Careful conditioning and appropriate choice of specimen thickness resulted in excellent resolution of the various features of the time dependence. The initial increase in oxygen flux reflected nonsteady-state diffusion. This part of the curve was controlled mainly by the diffusivity, D. As the permeant concentration in the specimen reached a constant

Table 1. Oxygen Barrier Properties of Cold-Crystallized PEN[a]

crystallization condition	density (g cm^{-3})	P	D	S	*trans* fraction	ΔH (J g^{-1})	ϕ_c	ρ_a (g cm^{-3})	S_a
quenched	1.3280 ± 0.0008	0.166 ± 0.004	1.51 ± 0.04	0.127 ± 0.001	0.21	1	0.01	1.327	0.128
165 °C, 10 min	1.3312 ± 0.0003	0.148 ± 0.006	1.32 ± 0.06	0.130 ± 0.001	0.24	7	0.05	1.325	0.137
165 °C, 16 min	1.3332 ± 0.0008	0.140 ± 0.001	1.30 ± 0.09	0.125 ± 0.008	0.25	9	0.06	1.326	0.133
165 °C, 30 min	1.3352 ± 0.0015	0.133 ± 0.005	1.21 ± 0.09	0.127 ± 0.004	0.27	14	0.10	1.323	0.141
165 °C, 45 min	1.3409 ± 0.0014	0.112 ± 0.001	1.03 ± 0.03	0.126 ± 0.004	0.33	25	0.18	1.318	0.153
165 °C, 52 min	1.3430 ± 0.0018	0.102 ± 0.004	0.97 ± 0.07	0.122 ± 0.004	0.36	28	0.20	1.318	0.152
165 °C, 1.0 h	1.3496 ± 0.0020	0.083 ± 0.001	0.86 ± 0.01	0.111 ± 0.001	0.42	39	0.28	1.313	0.155
165 °C, 2.0 h	1.3511 ± 0.0020	0.073 ± 0.001	0.75 ± 0.04	0.113 ± 0.005	0.47	42	0.30	1.311	0.161
165 °C, 8.0 h	1.3511 ± 0.0009	0.065 ± 0.003	0.67 ± 0.01	0.112 ± 0.007	0.47	43	0.31	1.310	0.162
165 °C, 13.5 h	1.3527 ± 0.0009	0.062 ± 0.004	0.62 ± 0.09	0.115 ± 0.008	0.50	46	0.33	1.308	0.173
180 °C, 12.0 h	1.3541 ± 0.0011	0.057 ± 0.004	0.58 ± 0.02	0.114 ± 0.003	0.51	50	0.36	1.303	0.177
200 °C, 10.0 h	1.3561 ± 0.0013	0.050 ± 0.004	0.52 ± 0.04	0.111 ± 0.001	0.54	54	0.39	1.300	0.181

[a] P, cm^3 (STP) cm m^{-2} atm^{-1} day^{-1}; D, $\times 10^{-13}$ m^2 s^{-1}; S and S_a, cm^3 (STP) cm^{-3} atm^{-1}.

Table 2. Oxygen Barrier Properties of Melt-Crystallized PEN[a]

crystallization condition	density (g cm^{-3})	P	D	S	*trans* fraction	ΔH (J g^{-1})	ϕ_c	ρ_a (g cm^{-3})	S_a
quenched	1.3280 ± 0.0008	0.166 ± 0.004	1.51 ± 0.04	0.127 ± 0.001	0.21	1	0.01	1.327	0.128
220 °C, 10 min	1.3287 ± 0.0016	0.156 ± 0.003	1.45 ± 0.03	0.125 ± 0.003	0.24	3	0.02	1.326	0.128
220 °C, 15 min	1.3324 ± 0.0020	0.139 ± 0.005	1.31 ± 0.02	0.123 ± 0.003	0.28	9	0.06	1.325	0.131
220 °C, 22 min	1.3360 ± 0.0011	0.121 ± 0.005	1.11 ± 0.04	0.126 ± 0.002	0.30	15	0.11	1.323	0.141
220 °C, 35 min	1.3399 ± 0.0020	0.102 ± 0.006	0.97 ± 0.02	0.122 ± 0.003	0.40	23	0.16	1.319	0.146
220 °C, 50 min	1.3453 ± 0.0013	0.086 ± 0.001	0.82 ± 0.01	0.121 ± 0.002	0.42	30	0.21	1.318	0.154
220 °C, 60 min	1.3508 ± 0.0015	0.065 ± 0.001	0.62 ± 0.02	0.121 ± 0.008	0.46	41	0.29	1.312	0.171
220 °C, 65 min	1.3542 ± 0.0012	0.057 ± 0.001	0.58 ± 0.03	0.114 ± 0.003	0.48	46	0.33	1.310	0.170
220 °C, 90 min	1.3559 ± 0.0008	0.052 ± 0.001	0.54 ± 0.01	0.111 ± 0.001	0.48	50	0.36	1.308	0.173
220 °C, 4.0 h	1.3575 ± 0.0012	0.050 ± 0.001	0.51 ± 0.03	0.113 ± 0.001	0.50	54	0.39	1.302	0.184

[a] P, cm^3 (STP) cm m^{-2} atm^{-1} day^{-1}; D, $\times 10^{-13}$ m^2 s^{-1}; S and S_a, cm^3 (STP) cm^{-3} atm^{-1}.

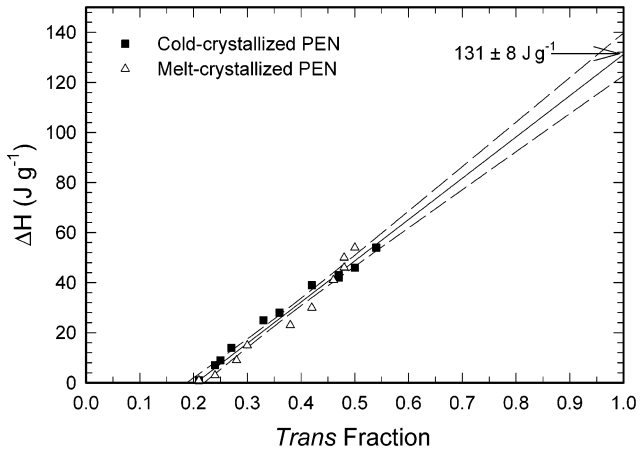

Figure 6. Relationship between ΔH and the *trans* fraction for cold- and melt-crystallized PEN.

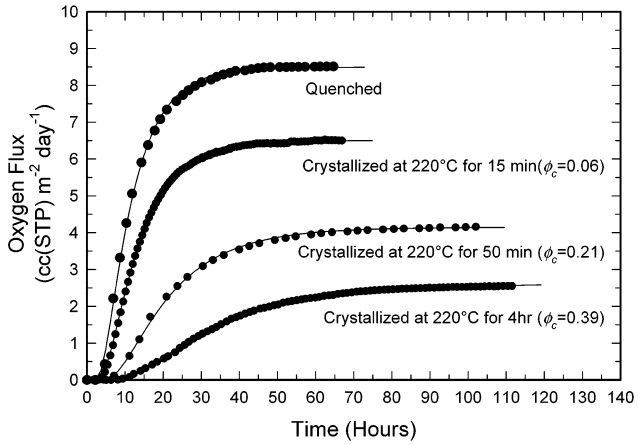

Figure 7. Experimental oxygen flux of melt-crystallized PEN normalized to a film thickness of 200 μm and the fit to eq 1.

distribution, the flux reached the steady-state value, J_o. This value, normalized to both the film thickness, l, and the permeant gas pressure, p, defined the permeability, $P = J_o l p^{-1}$. Crystallization affected both the non-steady-state and steady-state parts of the oxygen flux curve. The non-steady-state region broadened (slower diffusion), and the flux decreased (lower permeability).

To obtain the diffusivity, D, and to accurately determine the permeability, P, the data were fit to the solution of Fick's second law with appropriate boundary conditions:[7]

$$J(t) = \frac{Pp}{l}\left[1 + 2\sum_{n=1}^{\infty}(-1)^n \exp\left(-\frac{D\pi^2 n^2 t}{l^2}\right)\right] \qquad (1)$$

The fitting curves are included with the experimental points in Figure 7. The fit was equally good for all the experiments in the study. As indicated previously,[7] the error in determining the two fitting parameters P/l and D/l^2 was estimated not to exceed 2%. The low sensitivity of the flux to thickness variation within 30% was demonstrated previously.[7] Therefore, the accuracy of P and D was determined mainly by the accuracy of the average thickness measurement. For this reason, special attention was paid to the average thickness measurement as described in the Experimental Section. Solubility, S, was calculated from the relationship $S = PD^{-1}$.

The effect of cold and melt crystallization on the oxygen barrier properties of PEN is shown in Figure 8, with crystallinity expressed as density. Cold and melt crystallization reduced P similarly. In both cases the highest crystallinity achieved decreased P from 0.166 to about 0.050 cm^3 (STP) cm m^{-2} day^{-1} atm^{-1}, Tables 1 and 2. The improved barrier of crystallized PEN was almost entirely due to a decrease in D. At the highest

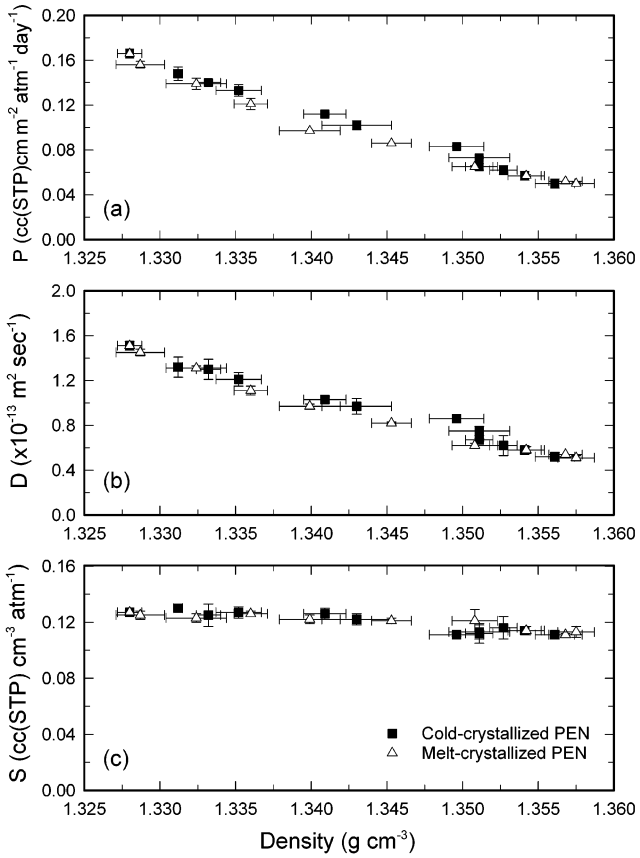

Figure 8. Effect of crystallinity as density on oxygen-transport parameters of PEN: (a) permeability; (b) diffusivity; (c) solubility.

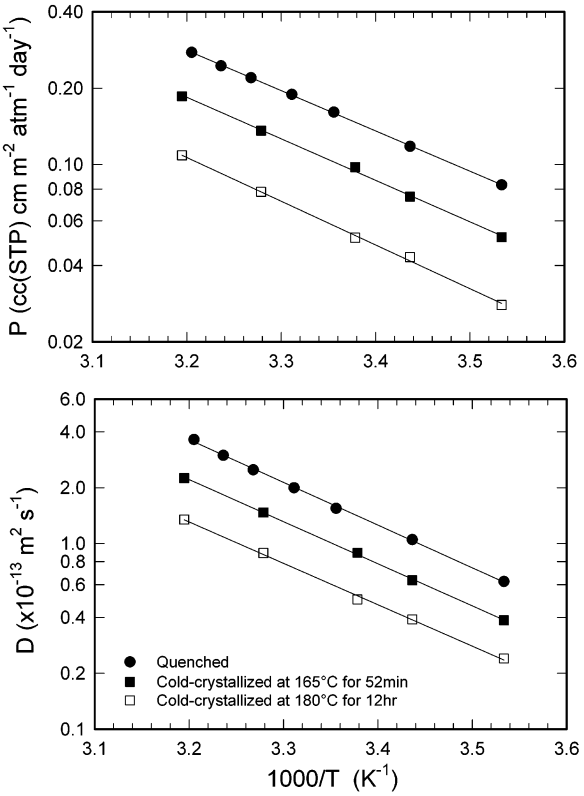

Figure 9. Temperature dependence of P and D for PEN.

crystallinity, D decreased from 1.51×10^{-13} to about 0.51×10^{-13} m^2 s^{-1}, Tables 1 and 2. Crystallization had almost no effect on S, which remained virtually constant at the value for amorphous PEN of 0.127 cm^3 (STP) cm^{-3} atm^{-1}.

The temperature dependence of P and D is shown in Figure 9 for an amorphous PEN film and cold-crystallized PEN films of intermediate and high crystallinity. An Arrhenius relationship was exhibited, and the resulting activation energies for oxygen permeation, E_P, and diffusion, E_D, are presented in Table 3. For these films, E_D decreased slightly as the crystallinity increased.

Discussion

Oxygen Sorption. The transport behavior of a crystalline polymer is often considered in terms of a two-phase structure consisting of an impermeable crystalline phase dispersed in a permeable amorphous matrix. Thus, both sorption and diffusion are seen as taking place in the amorphous phase. Solubility in the amorphous phase, S_a, is obtained by normalizing the measured bulk solubility, S, to the volume fraction of the amorphous phase:

$$S_a = \frac{S}{1 - \phi_c} \tag{2}$$

where ϕ_c is the volume fraction of crystallites. Sometimes S_a is independent of the amount of crystallinity, for example, in polyethylene.[4,25,26] In this case, S decreases in proportion to the crystallinity. However, in other cases, for example, in PET[7,9] and its copolymers,[8] S_a is found to increase with crystallinity. The fact that the bulk solubility, S, of PEN does not decrease with crystallinity as measured by density (Figure 8) suggests that PEN falls in the category of PET.

Following the approach used with PET,[27] analysis was carried out with a two-phase model with constant crystalline-phase density, ρ_c, and variable amorphous-phase density, $\rho_a(\rho)$. For a given bulk density, ρ, the value of ρ_a is obtained from the expression

$$\rho = \rho_c\phi_c + \rho_a(1 - \phi_c) \tag{3}$$

The volume fraction crystallinity, ϕ_c, in eqs 2 and 3 is determined by

$$\phi_c = \frac{\Delta H}{\Delta H^\circ}\frac{\rho}{\rho_c} \tag{4}$$

where ΔH is obtained from the DSC heating scan and ΔH° is the heat of melting of the perfect crystal.

The key to obtaining ρ_a is the choice of values for ΔH° and crystal density, ρ_c. Two crystal forms have been described for PEN; crystallization can take the α or β form depending on thermal history.[28,29] The α crystal form shows three strong reflections at 2θ values of 15.6°, 23.3°, and 27.0°, corresponding to the (010), (100), and ($\bar{1}$10) diffraction planes, and the β crystal form shows strong reflections at 2θ of 16.4°, 18.6°, and 25.5°, corresponding to the ($\bar{1}\bar{1}$0), (020), and (2$\bar{4}$2) diffraction planes.[20,29,30] Wide-angle X-ray diffraction confirmed that the barrier specimens crystallized in the α form. The presence of only the α crystal form was consistent with the findings of a previous study of PEN crystallization kinetics under equivalent conditions.[10] For the

Table 3. Activation Energies for Oxygen Permeation and Diffusion in PEN

sample	density (g cm^{-3})	ϕ_c	E_P (kJ mol^{-1})	E_D (kJ mol^{-1})
quenched	1.3280 ± 0.0008	0.01	29.7	44.1
cold-crystallized, 165 °C, 52 min	1.3430 ± 0.0018	0.20	31.3	43.4
cold-crystallized, 180 °C, 12.0 h	1.3541 ± 0.0011	0.36	33.0	42.8

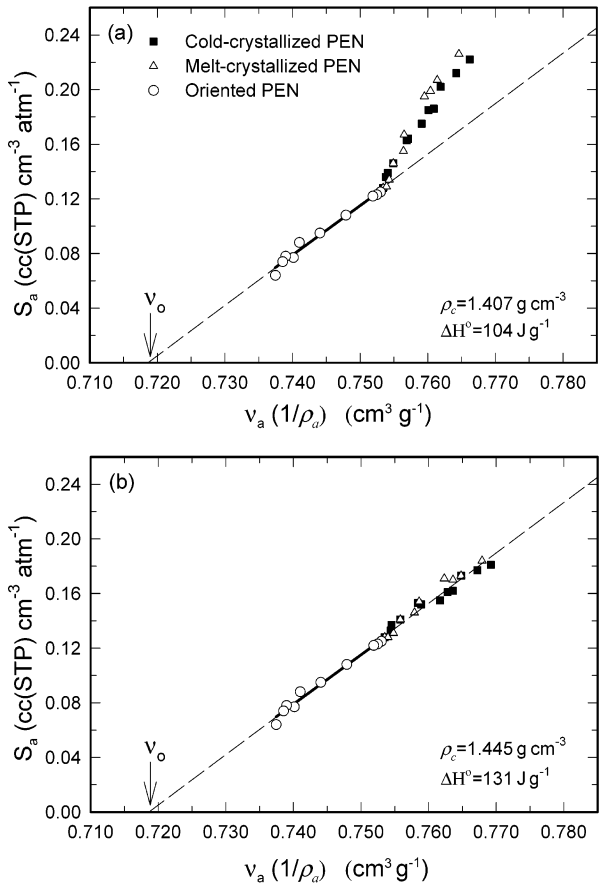

Figure 10. S_a versus ν_a for cold- and melt-crystallized PEN: (a) ρ_c = 1.407 g cm^{-3} and $\Delta H°$ = 104 J g^{-1}; (b) ρ_c = 1.458 g cm^{-3} and $\Delta H°$ = 131 J g^{-1}.

PEN α form, the reported unit cell density of 1.407 g cm^{-3} is widely used.[28] The relationship between amorphous solubility, S_a, calculated from eq 2 and amorphous-phase specific volume, $\nu_a = \rho_a^{-1}$, from eq 3 using a ρ_c of 1.407 g cm^{-3} and the reported value for $\Delta H°$ of 104 J g^{-1} [24] is plotted in Figure 10a.

A linear relationship between S_a and ν_a obtained under isothermal (25 °C) and isobaric (1 atm) conditions has been observed for crystallized PET,[7] for glassy copolymers of PET,[31,32] and for cold-drawn PEN, PET, and a PET copolymer.[21] The linear relationship appears to be a common characteristic of polyesters of ethylene glycol and aromatic diacids. The general correlation between S_a and ν_o is expressed as

$$S_a = \beta(\nu_a - \nu_o) \tag{5}$$

where ν_o is the specific volume at zero solubility. According to free volume concepts that view sorption as the process of filling holes of static free volume, the quantity $\nu_a - \nu_o$ identifies the excess-hole free volume available to oxygen.[21,31] Orientation of the glassy state decreases the excess-hole free volume, whereas crystallization often has the effect of increasing the excess-hole free volume of the amorphous phase. The extrapolated quantity ν_o is not necessarily the same for all polyesters and reflects a characteristic of the particular chemical structure. However, the slope β is about 3.6 cm^3 (STP) g cm^{-6} atm^{-1} for all the aromatic polyesters studied. The slope reflects the density of sorbed oxygen,[31] and constant β indicates fundamental similarity in the characteristics of the accessible free volume in the amorphous phase.

The dashed line in Figure 10a is the S_a versus ν_a correlation previously obtained for oriented glassy PEN.[21] Results for crystalline PEN lie considerably above the line. According to the present interpretation of eq 5, deviation from the established S_a versus ν_a correlation implies that accessible free volume in the amorphous phase of crystalline PEN is fundamentally different from accessible free volume in oriented PEN and in aromatic polyesters generally. A linear fit of the data as plotted in Figure 10a extrapolates to a zero solubility specific volume that is much larger than expected (less accessible free volume) and a density of sorbed oxygen that is much higher than expected on the basis of many previous observations. On the contrary, PALS revealed no differences in free volume hole radii among amorphous, crystallized, and oriented PEN. From analysis of the positron lifetime spectra in terms of three exponential components, the longest component τ_3, which characterizes the annihilation of orthopositronium, was 1.66, 1.65, and 1.62 ps for amorphous, crystalline, and oriented PEN, respectively, corresponding to hole radii of 2.51, 2.50, and 2.47 Å. The inconsistencies between observed permeation and PALS results were difficult to explain.

Alternatively the values of ρ_c and $\Delta H°$ used in eqs 2−4 could have been incorrect. To test this possibility, the value of ρ_c was adjusted to fit the data to the dashed line relationship first using a $\Delta H°$ of 104 J g^{-1} from the literature[24] and then using a $\Delta H°$ of 131 J g^{-1} from extrapolation of ΔH to 100% trans conformers (Figure 6). The former value of $\Delta H°$ resulted in amorphous specific volumes for crystalline PEN that were unrealistically high. The latter value of $\Delta H°$ gave the fit shown in Figure 10b with a crystal density, ρ_c, of 1.445 g cm^{-3}. Although considerably larger than the generally accepted value of the α form crystalline density, this value is not unreasonable. Indeed, it is very close to the density of 1.458 g cm^{-3} recently obtained by a refined analysis of the α form crystal structure.[33] Furthermore, a value larger than the crystal density of the β form (1.439 g cm^{-3})[29] is consistent with estimates of unit cell dimensions from molecular simulation.[34]

The quantities ϕ_c, ρ_a, and S_a obtained using a $\Delta H°$ of 131 J g^{-1} and a ρ_c of 1.445 g cm^{-3} are summarized in Tables 1 and 2. A plot of amorphous density, ρ_a, as a function of bulk density, ρ, shows the strong tendency of PEN to densify during crystallization, Figure 11. Corresponding data for PET from the literature[27] suggest that the densification effect is larger in PEN. Moreover, the trend for ρ_a of PET to level off at higher densities obtained at higher crystallization tempera-

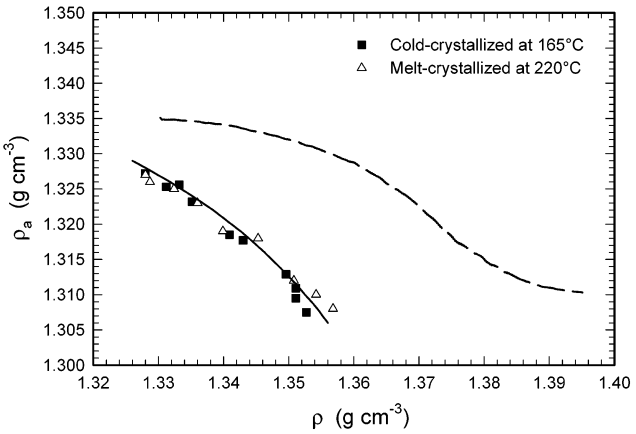

Figure 11. Amorphous density plotted versus bulk density for cold-crystallized and melt-crystallized PEN. The solid curve is from eq 15. The dashed curve is a fit to data for PET presented in ref 27.

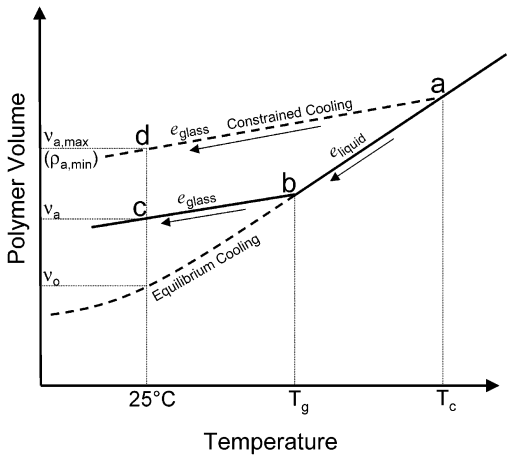

Figure 12. Representation of the volume−temperature relationship for unconstrained and constrained cooling of amorphous PEN.

tures was not detected in PEN for the crystallization conditions used in this study.[27]

Dedensification, or the increase in specific volume of the amorphous phase with crystallization, is attributed to constraint on relaxation of amorphous chain segments imposed by their attachment to chain segments in crystals. The phenomenon is analogous to that described previously for isothermally crystallized PET,[9] and for oriented PET crystallized under conditions where the rate of crystallization is fast compared to the rate of molecular relaxation.[35] The effect of constraint can be discussed in terms of the temperature−volume relationship for an amorphous polymer in Figure 12. As the polymer is cooled from the crystallization temperature, unconstrained amorphous chains contract along the equilibrium liquid line to the glass transition (*ab*) and then along the solid line to 25 °C (*bc*). However, amorphous chain segments that are attached to chain segments in crystals lack mobility to relax along the liquid line; instead they are immobilized much as they would be in the glassy state, and during cooling from the crystallization temperature they contract along a line parallel to the glass line (*ad*).

The additional free volume resulting from constraint, $\Delta\nu_f$, is the difference between the maximum dedensified amorphous specific volume, ν_{max}, and the specific volume of the unconstrained glass, ν_g (Figure 12). The maximum amorphous-phase specific volume is given by

$$\nu_{max} = \nu_g + \Delta\nu_f = \nu_g + \Delta e(T_c - T_g) \qquad (6)$$

where Δe is the difference between the specific thermal expansivities of equilibrium liquid and glass, $\Delta e = e_l - e_g$, with $e_l = 4.9 \times 10^{-4}$ cm^3 g^{-1} °C^{-1} for PEN[36] and, assuming e_g is the same as for PET, $e_g = 2.4 \times 10^{-4}$ cm^3 g^{-1} °C^{-1}.[36] In addition, T_c is the crystallization temperature, and T_g is the glass transition temperature taken as 118 °C from DSC measurements.[10,24] Values of ν_{max} and $\rho_{min} = (\nu_{max})^{-1}$ from eq 6 for four crystallization temperatures are given in Table 4 together with experimental ν_a and ρ_a values from eq 3 for barrier films with the longest crystallization times. The higher the crystallization temperature, T_c, the higher the value of ν_a at ambient temperature except for the film crystallized at 220 °C. The amorphous specific volume of the polymer fully crystallized at 165 °C matched the maximum value calculated from eq 6, Table 4. For crystallization at higher temperatures ν_a closely approached the maximum value ν_{max}. However, the experimental result was lower than the calculation by an amount that increased as the crystallization temperature increased. This could be ascribed to some relaxation of the constrained amorphous chain segments during cooling from the higher crystallization temperatures. Also, the crystallization time at 220 °C may not have been long enough to achieve maximum crystallinity.

Oxygen Diffusivity. Dedensification of the amorphous phase also affects the dynamic free volume; however, the effect of dedensification on diffusivity is superimposed on the large decrease that results from geometrical impedance to the transport path imposed by impermeable crystallites. Previous estimates suggest that dedensification increases the diffusivity of the amorphous phase of crystalline PET by about 20%; moreover, copolymerization with naphthalate appears to enhance the effect.[8] The diffusivity of dedensified amorphous PEN was estimated from the relationship between the diffusivity of an amorphous polymer, D_a, and the fractional free volume (FFV):[37−39]

$$D_a \propto \exp[-(B/\mathrm{FFV})] \qquad (7)$$

where the constant B characterizes the size of the opening between polymer chains required for the penetrant molecule to pass, which increases rapidly with the size of the permeant molecule, and FFV is defined as

$$\mathrm{FFV} = \frac{\nu_a - \nu_o}{\nu_a} \qquad (8)$$

where ν_o is taken as the zero solubility specific volume determined by the intercept in Figure 10b. Although first developed for rubbery polymers, eq 7 was subsequently applied to glassy polymers as well.[40−43] Previously, considerable scatter was encountered in applying eq 7 to large databases encompassing diffusion of various gases in a variety of glassy polymers.[44] However, by limiting the analysis to the diffusivity of a single gas in one amorphous polymer, an excellent linear correlation was obtained between ln D_a and FFV for oxygen diffusion in PEN, Figure 13. The plot was constructed with data from the previous study[21] in which cold-drawing decreased the FFV of amorphous PEN. It should be noted that this analysis neglects the effect of

Table 4. Amorphous-Phase Properties of Crystalline PEN

	experimental results					from eq 6		
crystallization temp (°C)	crystallization time (h)	ρ_a (g cm^{-3})	v_a (cm^3 g^{-1})	Δv_f (cm^3 g^{-1})	D_a ($\times 10^{-13}$ m^2 s^{-1})	ρ_{min} (g cm^{-3})	v_{max} (cm^3 g^{-1})	Δv_f (cm^3 g^{-1})
165	13.5	1.308	0.765	0.012	2.5	1.308	0.765	0.012
180	12.0	1.302	0.767	0.014	2.8	1.301	0.769	0.016
200	10.0	1.300	0.769	0.016	2.9	1.293	0.774	0.021
220	4.0	1.302	0.768	0.015	2.8	1.285	0.779	0.026

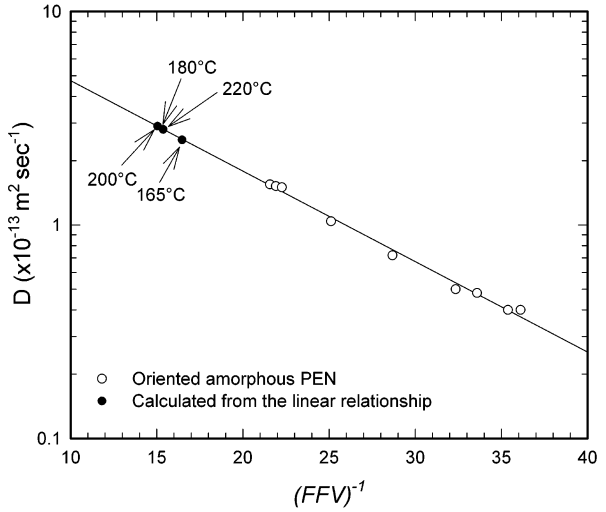

Figure 13. Relationship between amorphous diffusivity and fractional free volume. Data for oriented PEN are from ref 21.

anisotropy on D. Locating the dedensified amorphous density of fully crystallized PEN on the plot gave the D_a values listed in Table 4. A typical value of 2.8×10^{-13} m^2 s^{-1} represented an increase of almost 100% over the diffusivity of an amorphous PEN film of 1.51×10^{-13} m^2 s^{-1}.

It is possible to test whether this result is reasonable. The diffusivity of gases in glassy polymers typically follows the Arrhenius relationship for an activated process:

$$D = D_o \exp[-(E_D/RT)] \tag{9}$$

where E_D is the activation energy required to generate an opening between polymer chains large enough to allow the penetrant molecule to pass. The increase in amorphous diffusivity due to dedensification should result in a change in activation energy given by

$$\Delta E_D = RT \ln[D_a/D_a^o] \tag{10}$$

where D_a^o and D_a are the diffusivities before and after dedensification. If the diffusion mechanism is conserved and the change in jump length is small, D_o can be assumed constant.[45] For an increase in diffusivity from $D_a^o = 1.51 \times 10^{-13}$ m^2 s^{-1} for the amorphous film to $D_a = 2.8 \times 10^{-13}$ m^2 s^{-1} for the dedensified amorphous phase of PEN fully crystallized at 180 °C, a decrease in E_D of 1.5 kJ mol^{-1} is calculated from eq 10. This represents a decrease in E_D from 44.1 to 42.6 kJ mol^{-1}, which is very close to the 42.8 kJ mol^{-1} reported in Table 3. It should be reiterated that the D_a of dedensified PEN is an "intrinsic diffusivity" of the amorphous phase and does not include the effects of geometrical impedance imposed by the presence of crystals, which will strongly decrease the effective diffusivity of crystallized PEN.

Structural Model for Crystalline PEN. Morphologically, both cold and melt crystallization of PEN proceed by nucleation and growth of spherulites until the spherulites are space-filling.[10] This is shown schematically in Figure 14. A further increase in crystallinity is possible by secondary crystallization. When isothermal crystallization is arrested before the spherulites are space-filling by quenching below the glass transition temperature, PEN can be viewed morphologically as a dispersion of spherulites in a continuous amorphous matrix. However, the impermeable units of crystallized PEN are lamellar crystals, not spherulites. The individual spherulite is itself a composite structure consisting of impermeable lamellar crystals arranged in a permeable interlamellar amorphous phase. The interlamellar amorphous phase experiences constraint by the crystals, and therefore is expected to differ from the amorphous matrix in terms of density and transport properties.

The amorphous density, ρ_a, extracted from eq 3 and given in Tables 1 and 2 combines the characteristics of the amorphous matrix and the interlamellar amorphous phase. According to the structural model, the decrease in ρ_a as crystallinity increases should not be interpreted as the gradual dedensification of a homogeneous amorphous phase. Rather, dedensification arises from constraint imposed by crystallites on the interlamellar amorphous phase of the spherulites. As volume fraction crystallinity increases, the change in ρ_a averages the gradual increase in the amount of dedensified interlamellar amorphous phase and corresponding decrease in the amount of amorphous matrix. Similarly, S_a averages the oxygen solubilities in the amorphous matrix and in the dedensified interlamellar regions.

For simplicity, the volume crystallinity of the spherulites, ϕ_s, is assumed constant during spherulite growth, which is identified as the region of rapidly increasing ϕ_c in Figure 1. The point in Figure 1 where ϕ_c starts to level off gives $\phi_s = 0.30$ for cold crystallization at 165 °C and $\phi_s = 0.36$ for melt crystallization at 220 °C. The small increase in ϕ_c at longer times is attributed to increasing ϕ_s of space-filling spherulites due to secondary crystallization. The following discussion is limited to primary crystallization. Assuming that the density of the amorphous matrix, ρ_{am}, is the same as the density of amorphous PEN (1.328 g cm^{-1}) and that the dedensified interlamellar amorphous phase has constant density, ρ_{as}, a relationship between ρ_a from solubility and volume fraction crystallinity, ϕ_c, can be developed with ρ_{as} as the only unknown. Beginning with

$$\phi_a \rho_a = \rho_{am}(\phi_a - \phi_{as}) + \rho_{as}\phi_{as} \tag{11}$$

where ϕ_{as} is the volume fraction of the interlamellar amorphous phase, and noting that

$$\phi_{as} = \left[\frac{1 - \phi_s}{\phi_s}\right]\phi_c \tag{12}$$

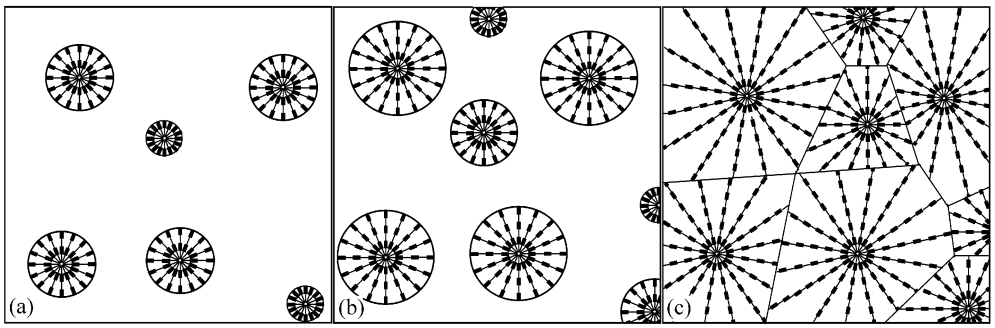

Figure 14. Schematic representation of the compact banded spherulites of isothermally crystallized PEN. V_s is the volume fraction occupied by spherulites.

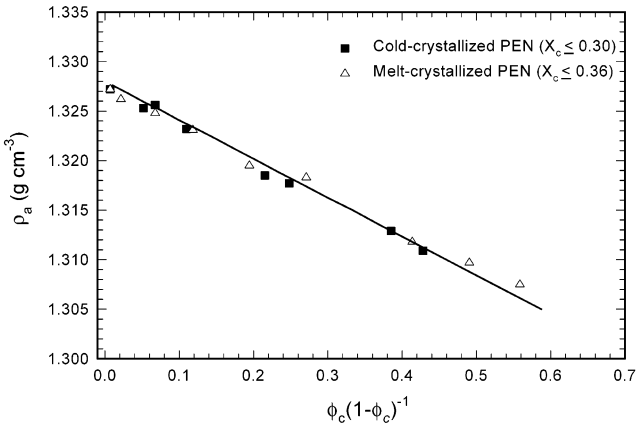

Figure 15. Relationship between amorphous-phase specific volume and crystallinity for the three-phase model. For cold crystallization $\rho_a = 1.328$ g cm^{-1}, $\rho_{as} = 1.311$ g cm^{-3}, and $\phi_s = 0.30$. For melt crystallization $\rho_a = 1.328$ g cm^{-1}, $\rho_{as} = 1.306$ g cm^{-3}, and $\phi_s = 0.36$.

and $\phi_a = 1 - \phi_c$, it follows that

$$\rho_a = \rho_{am} - \frac{\phi_c}{1-\phi_c}\left[\frac{1-\phi_s}{\phi_s}\right](\rho_{am} - \rho_{as}) \qquad (13)$$

A linear relationship between ρ_a and the quantity $\phi_c(1 - \phi_c)^{-1}$ in Figure 15 indicates that a constant value of ρ_{as} independent of the amount of crystallinity satisfactorily describes the change in the amorphous density of crystallized PEN. Values of ϕ_s given above result in a ρ_{as} of 1.311 g cm^{-3} for cold crystallization at 165 °C and 1.306 g cm^{-3} for melt crystallization at 220 °C, Table 5. These are only slightly higher than the amorphous-phase densities of fully crystallized PEN of 1.308 and 1.302 g cm^{-3}, respectively (Table 4). Secondary crystallization with increasing ϕ_s can impart further constraint and dedensification of the interlamellar amorphous phase. Nevertheless, the effect of secondary crystallization is small.

The structural model for permeation with three phases of constant density constitutes a refinement of the two-phase model with an impermeable crystalline phase and a permeable amorphous phase of variable density. By providing a structural basis for the apparent variation in amorphous-phase density, the three-phase model describes the relationship between measured density and effective amorphous density, something that was not possible with the empirical two-phase model. By combining eq 3 with eq 13, the amorphous density is given as

$$\rho_a = \frac{\rho_{am} - \rho\chi}{1-\chi} \qquad (14)$$

where

$$\chi = \left[\frac{1-\phi_s}{\phi_s}\right]\left[\frac{\rho_{am} - \rho_{as}}{\rho_c - \rho}\right] \qquad (15)$$

Using values given above for spherulite crystallinity, ϕ_s, and phase densities ρ_{am}, ρ_{as}, and ρ_c, the results from eq 15 are included in Figure 11 as essentially overlapping curves for cold-crystallized and melt-crystallized PEN.

Structural Model for Permeability. The generalized Maxwell model for gas transport in heterogeneous media describes the compositional dependence of permeability in systems with a less permeable phase dispersed in a higher permeability matrix.[46−48] The permeability is given by

$$P = P_c\left[1 + \frac{\phi_d(1+G)}{\left[\frac{(P_d/P_c)+G}{(P_d/P_c)-1}\right] - \phi_d}\right] \qquad (16)$$

where the subscripts "d" and "c" refer to the dispersed phase and continuous phase, respectively, and ϕ_d is the volume fraction of the dispersed phase. In this expression, G is a geometric factor that accounts for the shape of the dispersed phase. Although initially developed for a dilute dispersion of spheres, eq 16 has been shown to be valid over the entire composition range.[49]

Considering crystallized PEN as a dispersion of less permeable spherulites in a more permeable amorphous matrix, the Maxwell equation can be used to describe permeability. Assuming a constant volume crystallinity of spherulites, ϕ_s, during spherulite growth, increasing the bulk volume crystallinity, ϕ_c, increases the volume fraction occupied by spherulites as $V_s = \phi_c/\phi_s$. When the spherulites are space-filling, V_s is equal to unity and $\phi_s = \phi_c$. If it is further assumed that the permeability of the spherulites, P_s, is constant and does not change with V_s, and the permeability of the amorphous matrix, P_a, is equal to the permeability of the amorphous PEN film, the Maxwell equation with a G of 2 for a spherical dispersion takes the form

Table 5. Physical Properties of PEN Spherulites[a]

sample	ρ_{as} (g cm^{-3})	P_{as}	S_{as}	D_{as}	ϕ_s	ρ_s (g cm^{-3})	P_s	S_s	D_s	α
cold-crystallized at 165 °C	1.311	0.338	0.163	2.4	0.30	1.351	0.075	0.114	0.76	18
melt-crystallized at 220 °C	1.306	0.391	0.174	2.6	0.36	1.356	0.048	0.111	0.50	20

[a] P_{as} and P_s, cm^3 (STP) cm m^{-2} atm^{-1} day^{-1}; D_{as} and D_s, $\times 10^{-13}$ m^2 s^{-1}; S_{as} and S_s, cm^3 (STP) cm^{-3} atm^{-1}.

$$P = P_a\left[1 + \frac{3V_s}{\left[\frac{(P_s/P_a)+2}{(P_s/P_a)-1}\right] - V_s}\right] \tag{17}$$

with P_s as the single fitting parameter.

The quantity P/P_a is plotted versus V_s in Figure 16 for crystallized PEN in the primary crystallization region where $\phi_c \leq \phi_s$. The solid line fits show that eq 17 satisfactorily describes the effect of crystallization with a constant P_s of 0.075 cm^3 (STP) cm m^{-2} atm^{-1} day^{-1} for cold crystallization at 165 °C, and a P_s of 0.048 cm^3 (STP) cm m^{-2} atm^{-1} day^{-1} for melt crystallization at 220 °C. Not surprisingly, the higher crystallization temperature yields better spherulitic organization and consequently larger ϕ_s and lower P_s.

The impermeable structural element of the spherulite is the lamellar crystal. An AFM phase image of crystallized PEN shows stacks of twisted platelet-shaped lamellae, Figure 17. Structurally, this resembles the dispersion of impermeable platelets of given aspect ratio that has been modeled by Cussler et al.[50−52] If the platelets are oriented at a fixed angle to the flux, the permeability of the composite is expressed as

$$P = P_m\left[1 + \frac{\alpha^2\phi^2}{4(1-\phi)}\cos^2\theta\right]^{-1} \tag{18}$$

where P_m is the permeability of the matrix, ϕ is the volume fraction of impermeable platelets, α is the aspect ratio of the platelets defined as length divided by width, and θ is the angle between the flux and the normal to the platelets.

For isotropic, space-filling spherulites, the lamellar orientation is averaged according to

$$\langle\cos^2\theta\rangle = 1/3 \tag{19}$$

and eq 18 becomes

$$P_s = P_{as}\left[1 + \frac{\alpha^2\phi_s^2}{12(1-\phi_s)}\right]^{-1} \tag{20}$$

where $P_{as} = D_{as}S_{as}$ refers to the permeability of the interlamellar amorphous regions of the spherulite. From Figure 10b the solubility of oxygen in the amorphous regions of the spherulite, S_{as}, is 0.163 and 0.174 cm^3 (STP) cm^{-3} atm^{-1} for cold-crystallized and melt-crystallized PEN, respectively. The diffusivity of oxygen in the amorphous regions of the spherulite, D_{as}, is obtained from the relationship between diffusivity and fractional free volume in Figure 13 and is 2.4×10^{-13} and 2.6×10^{-13} m^2 s^{-1} for cold-crystallized and melt-crystallized PEN, respectively. The resulting aspect ratio of the impermeable crystals is 18 for cold crystallization at 165 °C and 20 for melt crystallization at 220 °C. For lamellar crystals 30−40 nm thick the corresponding lamellar length would be approximately 700 nm. Despite the difficulty in determining the length of closely packed and twisting lamellae, the magnitude of the estimated lamellar length appears reasonable on the basis of the AFM images.

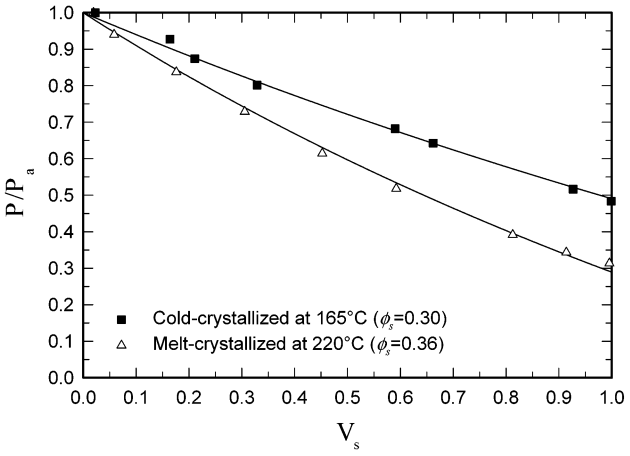

Figure 16. Relative permeability versus V_s for cold-crystallized and melt-crystallized PEN and the fit to the Maxwell model. For cold crystallization $P_s = 0.075$ cm^3 (STP) cm m^{-2} atm^{-1} day^{-1}; for melt crystallization $P_s = 0.048$ cm^3 (STP) cm m^{-2} atm^{-1} day^{-1}. $P_a = 0.166$ cm^3 (STP) cm m^{-2} atm^{-1} day^{-1}.

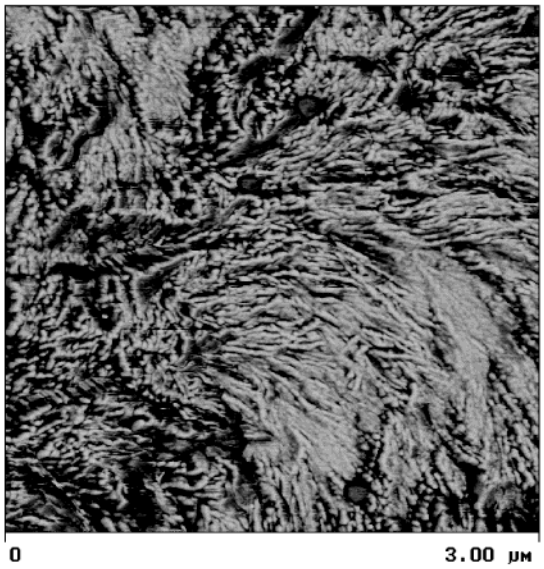

Figure 17. AFM phase image of PEN melt-crystallized at 220 °C for 90 min. The lamellar thickness is 30−40 nm, and the lamellar length is 700−1000 nm.

Conclusions

In the present study we test the formulation of the two-phase model for gas transport by examining the oxygen-transport properties of isothermally cold-crystallized and melt-crystallized PEN. Gas solubility provides the easiest test of the two-phase model; however, oxygen solubility in PEN does not exhibit the expected proportional decrease with volume fraction crystallinity. One approach is to modify the simple two-phase model of constant crystalline- and amorphous-phase densities to

incorporate a permeable amorphous phase of variable density. The resulting relationship between oxygen solubility and amorphous-phase density is consistent with free volume concepts that view sorption as the process of filling excess-hole free volume. However, this approach does not lead to a structural interpretation of the variable amorphous-phase density, nor does it provide an interpretation of the other transport parameters of diffusivity and the product, permeability.

Morphological observations provide the basis of a structural model that identifies a permeable amorphous matrix of constant density containing dispersed spherulites of lower permeability. The spherulites themselves are composites of impermeable crystallites and permeable interlamellar amorphous regions of lower density than the amorphous matrix. Dedensification of the interlamellar amorphous phase is due to the constrained nature of amorphous chains anchored to crystallites. The density of the unrelaxed interlamellar amorphous phase confirms the glassy nature of constrained chains at the crystallization temperature. This produces a three-phase model with constant densities. The structural model is reconciled with the two-phase transport model by noting that the variable amorphous-phase density of the two-phase model is a weighted average of the densities of the amorphous matrix and the interlamellar amorphous phase in the structural model.

The model provides a structural approach for interpreting gas-transport parameters. Solubility is seen as filling holes of static free volume. Dedensification of the interlamellar amorphous phase increases the excess-hole free volume available for oxygen sorption by an amount that is directly proportional to the increase in amorphous specific volume. The magnitude of the effect is large enough in PEN that the increase in solubility due to dedensification essentially offsets the decrease expected from the presence of impermeable crystallites, resulting in oxygen solubility that is essentially invariant with the level of crystallinity. Additionally, the structural model is the basis for applying the generalized Maxwell model for gas transport in heterogeneous systems consisting of a less permeable phase dispersed in a more permeable matrix. The analysis yields the basic oxygen-transport parameters of the spherulite. Thus, oxygen permeability of the spherulite is in the range of 30−50% that of the amorphous polymer. Further consideration of spherulite permeability provides an aspect ratio of impermeable crystallites that is consistent with the dimensions of platelet-shaped lamellae.

Acknowledgment. This research was generously supported by the National Science Foundation, Grants DMR 9975774 and DMR 9986467, and KoSa. Support from Modern Controls, Inc. for development of a facility for gas-transport studies at CaseWestern Reserve University is gratefully acknowledged.

References and Notes

(1) Vieth, W. R. *Diffusion In and Through Polymers*; Hanser: Munich, 1991; Chapter 4, pp 73−110.
(2) Hedenqvist, M.; Gedde, U. W. *Prog. Polym. Sci.* **1996**, *21*, 299−333.
(3) Weinkauf, D. H.; Paul, D. R. In *Barrier Polymers and Structures*; Koros, W. J., Eds.; American Chemical Society: Washington, DC, 1990; Chapter 3, pp 60−91.
(4) Michaels, A. S.; Bixler, H. J.; Fein, H. L. *J. Appl. Phys.* **1964**, *35*, 3165−3178.
(5) Lasoski, S. W., Jr.; Cobbs, W. H., Jr. *J. Polym. Sci.* **1959**, *36*, 21−33.
(6) Michaels, A. S.; Vieth, W. R.; Barrie, J. A. *J. Appl. Phys.* **1963**, *34*, 1−12.
(7) Sekelik, D. J.; Stepanov, S. V.; Nazarenko, S.; Schiraldi, D.; Hiltner, A.; Baer, E. *J. Polym. Sci., Part B: Polym. Phys.* **1999**, *37*, 847−857.
(8) Polyakova, A.; Stepanov, E. V.; Sekelik, D.; Schiraldi, D. A.; Hiltner, A.; Baer, E. *J. Polym. Sci., Part B: Polym. Phys.* **2001**, *39*, 1911−1919.
(9) Lin, J.; Shenogin, S.; Nazarenko, S. *Polymer* **2002**, *43*, 4733−4743.
(10) Hu, Y. S.; Rogunova, M.; Schiraldi, D. A.; Hiltner, A.; Baer, E. *J. Appl. Polym. Sci.* **2002**, *86*, 98−115.
(11) Lee, S. W.; Cakmak, M. *J. Macromol. Sci., Phys.* **1998**, *B37*, 501−526.
(12) Keller, A. In *Polymers, Liquid Crystals, and Low-Dimensional Solids*, March, N., Tosi, M., Eds.; Plenum: New York, 1984; Chapter 2, pp 33−69.
(13) Higuchi, H.; Yu, Z.; Jamieson, A. M.; Simha, R.; McGervey, J. D. *J. Polym. Sci., Part B: Polym. Phys.* **1995**, *33*, 2295−2305.
(14) Shabana, H. M.; Olley, R. H.; Basssett, D. C.; Zachmann, H. G. *J. Macromol. Sci., Phys.* **1996**, *B35*, 691−708.
(15) Keith, H. D.; Padden, F. J. *Macromolecules* **1996**, *29*, 7776−7786.
(16) Schulze, K.; Kressler, J.; Kammer, H. W. *Polymer* **1993**, *34*, 3704−3709.
(17) Ho, R.-M.; Ke, K.-Z.; Chen, M. *Macromolecules* **2000**, *33*, 7529−7537.
(18) Ouchi, I.; Hosoi, M.; Shimotsuma, S. *J. Appl. Polym. Sci.* **1977**, *21*, 3445−3456.
(19) Kimura, F.; Kimura, T.; Sugisaki, A.; Komatsu, M.; Sata, H. Ito, E. *J. Polym. Sci., Part B: Polym. Phys.* **1997**, *35*, 2741−2747.
(20) Vasanthan, N.; Salem, D. R. *Macromolecules* **1999**, *32*, 6319−6325.
(21) Liu, R. Y. F.; Schiraldi, D. A.; Hiltner, A.; Baer, E. *J. Polym. Sci., Part B: Polym. Phys.* **2002**, *40*, 862−877.
(22) Schmidt, P. G. *J. Polym. Sci., Part A: Gen. Pap.* **1963**, *1*, 1271−1292.
(23) Qureshi, N.; Stepanov, E. V.; Schiraldi, D.; Hiltner, A.; Baer, E. *J. Polym. Sci., Part B: Polym. Phys.* **2000**, *38*, 1679−1686.
(24) Cheng, S. Z. D.; Wunderlich, B. *Macromolecules* **1988**, *21*, 789−797.
(25) Michaels, A. S.; Parker, R. B., Jr. *J. Polym. Sci.* **1959**, *41*, 53−71.
(26) Michaels, A. S.; Bixler, H. J. *J. Polym. Sci.* **1961**, *50*, 393−412.
(27) Bornschlegl, E.; Bonart, R. *Colloid Polym. Sci.* **1980**, *258*, 319−331.
(28) Mencik, Z. *Chem. Prum.* **1967**, *17*, 78−81.
(29) Buchner, S.; Wiswe, D.; Zachmann, H. G. *Polymer* **1989**, *30*, 480−488.
(30) van der Heuvel, C. J. M.; Klop, E. A. *Polymer* **2000**, *41*, 4249−4266.
(31) Polyakova, A.; Liu, R. Y. F.; Schiraldi, D. A.; Hiltner, A.; Baer E. *J. Polym. Sci., Part B: Polym. Phys.* **2001**, *39*, 1889−1899.
(32) Polyakova, A.; Connor, D. M.; Collard, D. M.; Schiraldi, D. A.; Hiltner, A.; Baer, E. *J. Polym. Sci., Part B: Polym. Phys.* **2001**, *39*, 1900−1910.
(33) Liu, J.; Myers, J.; Geil, P. H.; Kim, J. C.; Cakmak, M. *ANTEC Proc.* **1997**, 1562−1566.
(34) Tonelli, A. E. *Polymer* **2002**, *43*, 637−642.
(35) Gohil, R. M. *J. Appl. Polym. Sci.* **1994**, *52*, 925−944.
(36) Van Krevelen, D. W. *Properties of Polymers*, 3rd ed.; Elsevier: Amsterdam, 1997; Chapter 4, pp 71−107.
(37) Cohen, M. H.; Turnbull, D. *J. Chem. Phys.* **1959**, *31*, 1164−1169.
(38) Fujita, H. *Fortschr. Hochpolym.-Forsch.* **1961**, *3*, 1−47.
(39) Takeuchi, H.; Okazaki, K. *J. Chem. Phys.* **1990**, *92*, 5643−5652.
(40) Duda, J. L.; Zielinski, J. M. In *Diffusion in Polymers*; Neogi, P., Ed.; Marcel Dekker: New York, 1996; Chapter 3, pp 143−171.
(41) Barbari, T. A.; Koros, W. J.; Paul, D. R. *J. Polym. Sci., Part B: Polym. Phys.* **1988**, *26*, 709−727.
(42) Hägg, M.-B.; Koros, W. J.; Schmidhauser, J. C. *J. Polym. Sci., Part B: Polym. Phys.* **1994**, *32*, 1625−1633.
(43) Park, J. Y.; Paul, D. R. *J. Membr. Sci.* **1997**, *125*, 23−39.
(44) Thran, A.; Kroll, G.; Faupel, F. *J. Polym. Sci., Part B: Polym. Phys.* **1999**, *37*, 3344−3358.
(45) Meares, P. *J. Am. Chem. Soc.* **1954**, *76*, 3415−3422.

(46) Petropoulos, J. H. *Adv. Polym. Sci.* **1985**, *64*, 93−142.
(47) Barrer, R. M. In *Diffusion in Polymers*; Crank, J., Park, G. S., Eds.; Academic: New York, 1968; Chapter 6, pp 165−217.
(48) Puleo, A. C.; Paul, D. R.; Wong, P. K. *Polymer* **1989**, *30*, 1357−1366.
(49) Petropoulos, J. H. *J. Polym. Sci., Polym. Phys. Ed.* **1985**, *23*, 1309−1324.
(50) Cussler, E. L.; Hughes, S. E.; Ward, W. J., III; Aris, R. *J. Membr. Sci.* **1988**, *38*, 161−174.
(51) Eitzman, D. M.; Melkote, R. R.; Cussler, E. L. *AIChE J.* **1996**, *42*, 2−9.
(52) Falla, W. R.; Mulski, M.; Cussler, E. L. *J. Membr. Sci.* **1996**, *119*, 129−138.

MA0205156